Post-Print

This is the accepted version of:

The final publication is available at https://doi.org/10.2514/6.2024-1268

Access to the published version may require subscription.

When citing this work, cite the original published paper.

Permanent link to this version
http://hdl.handle.net/11311/1259339

Experimental Identification and Control of Flutter beyond the First Flutter Mechanism

Francesco Toffol[1], Nicola Fonzi[2], Giampiero Bindolino[3], Sergio Ricci[4]
Politecnico di Milano, via La Masa 34, 20156 Milano, Italy

John Berg[5] and Eli Livne[6]
University of Washington, Seattle, WA 98195 – 2400

The results of wind tunnel flutter tests with an aeroservoelastic model of a full airplane configuration are presented. The model has two flutter mechanisms in the operative range of the wind tunnel. With a proper design of active control laws, it is possible to reach and experimentally identify the second flutter mechanism without modifying its behavior. A modified controller can control both flutter mechanisms and expand the flight envelope to 20% in airspeed above both mechanisms.

I. Introduction

The possibility of reaching and identifying in tests different flutter mechanisms is of interest, since input/output test results close to a flutter condition (and, in the case of very mild flutter, at the flutter condition) can help improve mathematical models in their capacity to capture, by analysis, the complex dynamic aeroelastic behavior of configurations that have multiple flutter mechanisms. In symmetric aircraft configurations, where the dynamics of the airplane can be separated into symmetric and antisymmetric dynamics, if the first symmetric flutter mechanism is reached before the first antisymmetric mechanism, it is not possible, using conventional methods, to reach that first antisymmetric mechanism in a test. Similarly, if the first antisymmetric mechanism is reached first, the first symmetric mechanism cannot be approached in a test, and experimental system identification close to that first symmetric mechanism cannot be carried out.

In the case of enough independent control surfaces on a configuration that is actively controlled, the theoretical possibility exists to reach a flutter mechanism by suppressing those mechanisms below it without affecting it. For this, certain modes of motion have to be made uncontrollable by the array of control surfaces that suppresses the lower modes, depending on their locations and whether they are activated or not.

But the symmetric flutter / antisymmetric flutter case is straightforward. Active flutter suppression of the symmetric dynamics will not affect the antisymmetric dynamics and vice versa.

In the work reported here an antisymmetric flutter mechanism of an aeroelastic wind tunnel model of a full aircraft was reached in a test after the symmetric flutter mechanism at a lower speed was suppressed using active control. System identification was carried out for both mechanisms close to where stability was lost. Active Flutter Suppression (AFS), then, beyond its role in stabilizing and removing flutter away from the flight envelope of a flexible configuration [1], can also be useful for exploring experimentally the different flutter mechanisms the configuration has and the associated fine-tuning of mathematical models.

II. Description of the X-DIA Model

The wind tunnel model is the revamped X-DIA aero-servo-elastic model described in [2]-[5]. It has a conventional low-mounted backward swept wing and a T-Tail. Its installation in the wind tunnel is shown in Figure 1(a). After the

---

[1] Researcher, Department of Aerospace Science and Technology.
[2] PhD Candidate, Department of Aerospace Science and Technology.
[3] Researcher, Department of Aerospace Science and Technology.
[4] Professor, Department of Aerospace Science and Technology, AIAA Associate Fellow.
[5] PhD student, William E. Boeing Department of Aeronautics and Astronautics.
[6] Professor, William E. Boeing Department of Aeronautics and Astronautics. AIAA fellow.

AFS tests performed in 2020, the tail was redesigned to study the effects of gaps (freeplay) in the elevators and rudder kinematics. This was done to create control surface induced Limit Cycle Oscillation (LCO) mechanisms and to study their effect on the aeroelastic behavior of the entire aircraft [6]-[8]. Since the LCO is extremely sensitive to the aircraft's incidence and sideslip angles because of associated pre-loads on the control surfaces [9]-[12], the cable-supported configuration of [2]-[5] was replaced by a pylon that connects the model to the wind tunnel floor and allows an accurate positioning of the model in the wind tunnel. The pylon can rotate around its axis (sideslip angle) and its head can be rotated up and down to define the angle of attack.

The aero-servo-elastic model is made of an internal metal (aluminum and steel) skeleton that provides the stiffness characteristics, the external surface is created by a set of aerodynamic sectors realized in honeycomb (fuselage) and 3D printed material (lifting and control surfaces). The model is equipped with a set of accelerometers to measure the response and to provide the feedback for the Active Flutter Suppression (AFS) laws. The ailerons are actuated by servomotors, while the elevators and rudder are not actuated. A dedicated mechanism is created to modify the freeplay gap of the tail's control surfaces. The tail's control surface rotation is measured by a set of encoders while the aileron positions are measured by encoders mounted on the servomotors. The servomotor controller is the one described in [13].

The wing tips are equipped with two pods that contain flutter stoppers. These are two sliding masses that can be moved forward by a pneumatic actuator when the measured accelerations exceed a given threshold, suppressing the flutter in a passive way by changing the dynamics of the model. Being able to automatically move the flutter stopper masses to their "flutter-safe" forward positions and then move them back, on command, to their rear positions for which flutter speeds are within the operating conditions of the tunnel makes it possible to reach flutter, back off, and then push towards it again without stopping the tunnel, which saves significant time during testing.

A Finite Element Method (FEM) math model was created using different element type (beam, plate and solid) for the structural elements. The aerodynamics is represented with two different math models: a classical Doublet-Lattice Method (DLM) model for the aeroelastic simulations and control laws design, and a 3D panel method based on Morino's method used to evaluate geometrical effects (especially those of bodies) as discussed in Sec. III-B.

The X-DIA model was analyzed using NeoCASS [14] because it embeds an automatic procedure for the State-Space (SS) model generation [15] that generates the unsteady aerodynamic forces transfer functions. NeoCASS does not have all the structural elements implemented in Nastran but it is possible to use the direct matrix i/o capability of Nastran DMIG [16]. For this reason, some portions of the model, like wings and their connections to the fuselage beam, were exported as DMIG from Nastran. The FEM-DLM interface is based on a set of surface splines, using the Radial Basis Function (RBF) technique [17]. A 2% of structural damping factor is added to each mode. The FEM model is shown in Figure 1 (b).

(a)   (b)
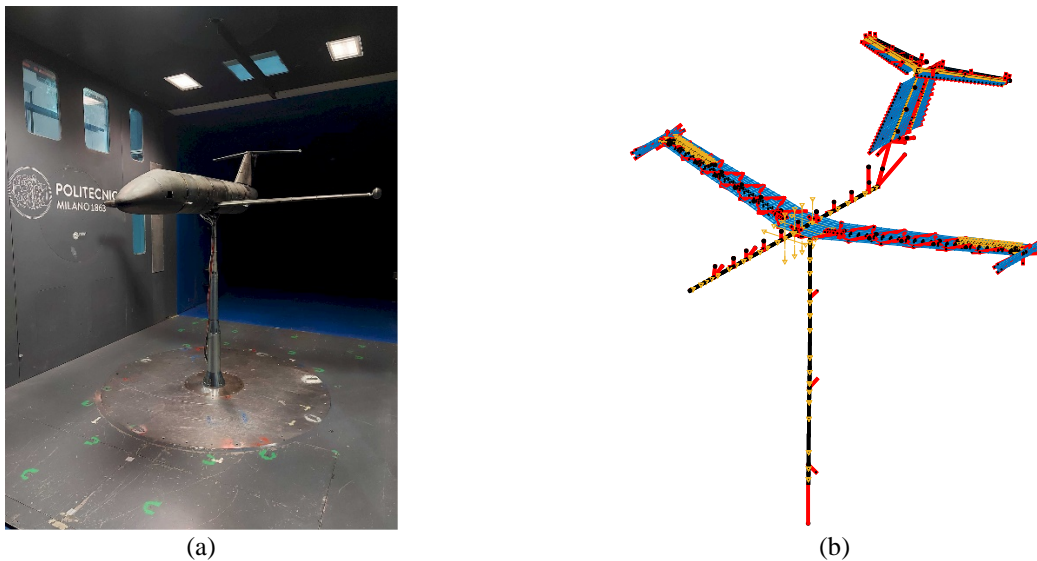
Figure 1: The aeroelastic model of F-XDIA mounted on the pylon (a) and the corresponding FEM model (b).

A Ground Vibration Test (GVT) was performed with the model mounted in the wind tunnel test section on the pylon and the FEM model was updated to match the measured modes in term of modal shapes and frequencies. The State-Space (SS) model realization is discussed in [4][5] and the same procedure was employed to generate the SS model of the pylon mounted X-DIA.

<p style="text-align:center">III.   Numerical analyses</p>

Standard methods of dynamic aeroelastic stability analyses were used. For the passive FEM model (control surfaces fixed) – the p-k method of NeoCASS [18] was used. The stability of the actively controlled model was evaluated by looking the real parts of the closed-loop state matrix eigenvalues as functions of airspeed. The SS model is fully representative of the FEM model, the control laws, and the actuator transfer functions. The damping ratios of the system's poles are expressed as $\xi_i = \frac{\Re(\lambda_i)}{|\lambda_i|}$.

A. Open loop flutter

The flutter analysis is performed for the model with the control surfaces fixed. The analysis was performed using the p-k method implemented in NeoCASS and provides the evolution of the aeroelastic eigenvalues (poles) λ real and imaginary parts with respect to the airspeed. The frequency, in Hz, is obtained from $f_i = \frac{|\lambda_i|}{2\pi}$, while the damping is obtained as $g_i = 2\frac{\Re(\lambda_i)}{|\lambda_i|}$. That is, twice the damping ratio ξ_i. The results can be graphically shown in V-f and V-g plots as in Figure 2 (with a zoom on the damping axis in Figure 3(a)). Both symmetric and antisymmetric flutter cases are shown, where the unstable branch in blue represents the symmetric instability and the unstable branch in green represents the antisymmetric instability. The two flutter instabilities occur at 41.5 m/s (symmetric bending-torsion) and 47 m/s (anti-symmetric bending torsion).
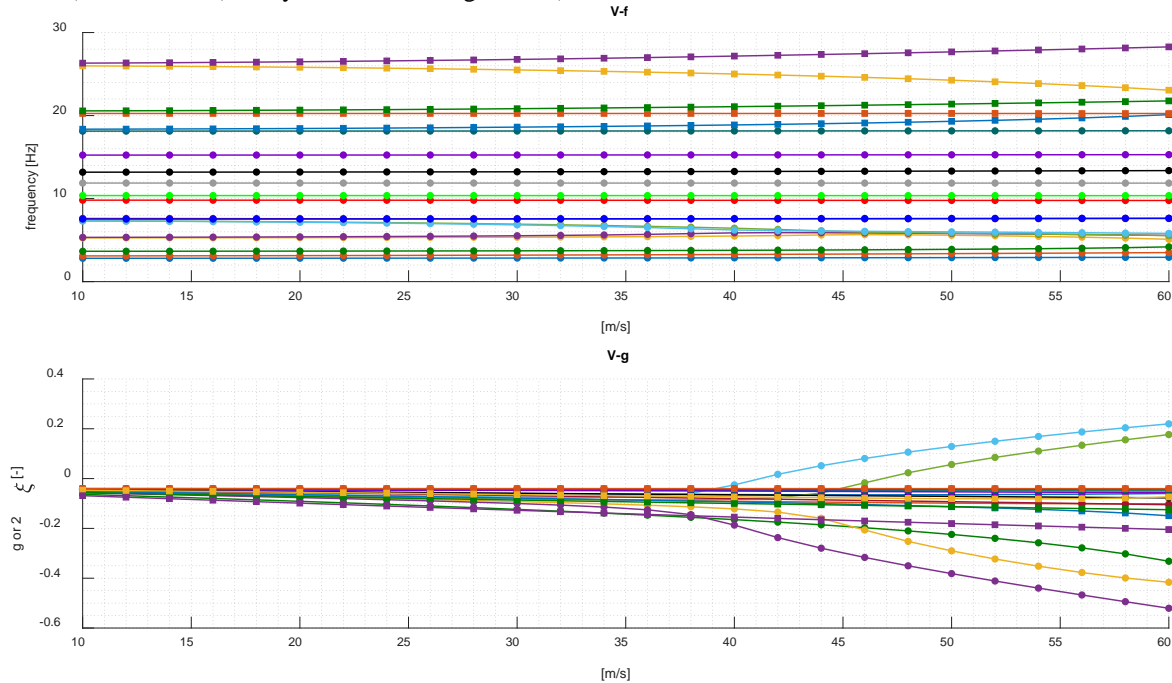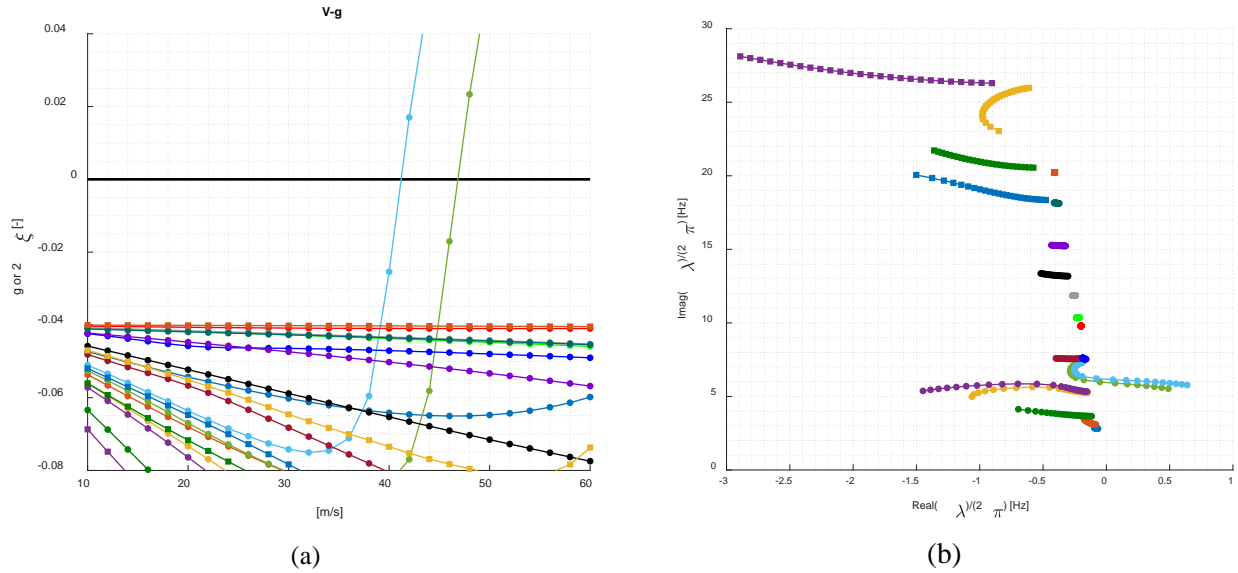

Figure 2: V-f and V-g diagram for the X-DIA model mounted on the pylon.

(a)   (b)

Figure 3: (a) Root Locus of the X-DIA model (b) V-g plot zoomed around the damping axis.

The root locus results for the passive (controls-locked) system are shown in Figure 3 (b), where the flutter point can be identified for the two branches when the real parts of the eigenvalues turns positive.

The flutter shapes for the two cases are shown in Figure 4(a) for the symmetric and Figure 4(b) for the anti-symmetric flutter mechanism. The two deformed shapes are evaluated at the correspondent flutter speeds of 41.5 m/s and 47 m/s

(a)   (b)
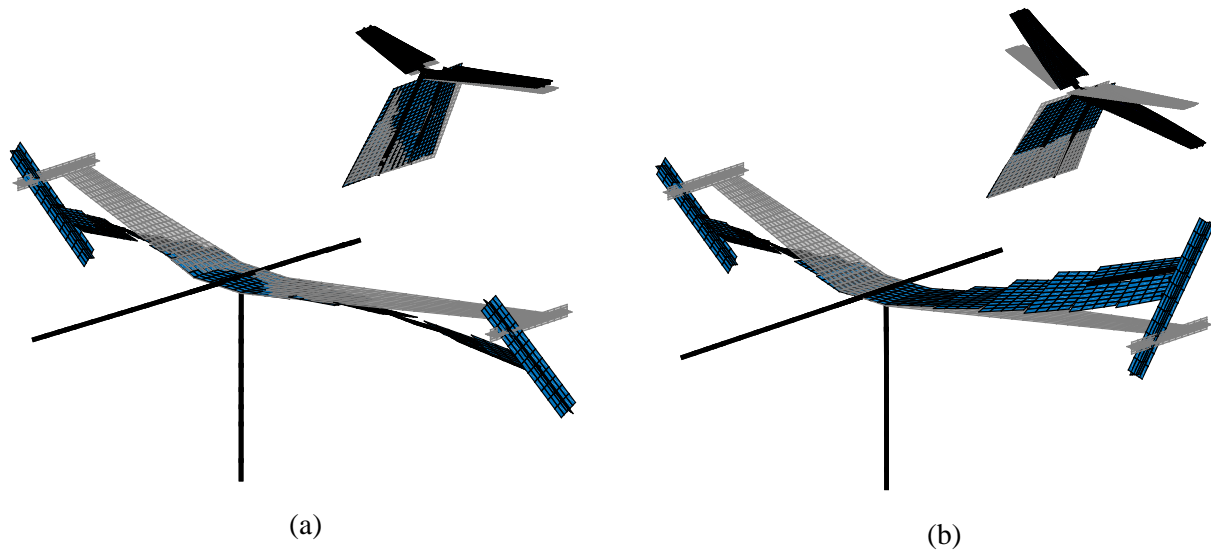
Figure 4: Symmetric torsion-bending (a) and anti-symmetric torsion-bending (b) flutter mechanisms.

B. Open Loop Flutter with 3D panel method

To better investigate the impact of the tip pods on the flutter phenomenon, the classic DLM used for the computation of the unsteady aerodynamic forces was substituted with an in hause 3D panel method named ALIS. It is based on the Morino's 3D panel method and it is described in [19]. The complete mesh is shown in Figure 5(a).

4

In particular, three different math models have been developed and compared. The complete X-DIA model on the pylon, without the tip pods; a second one with the tip pods directly connected to the wing mesh, and a third one where between the wing and the pods there is a small gap (see Figure 5 (b)), as it is in the reality.

(a)   (b)
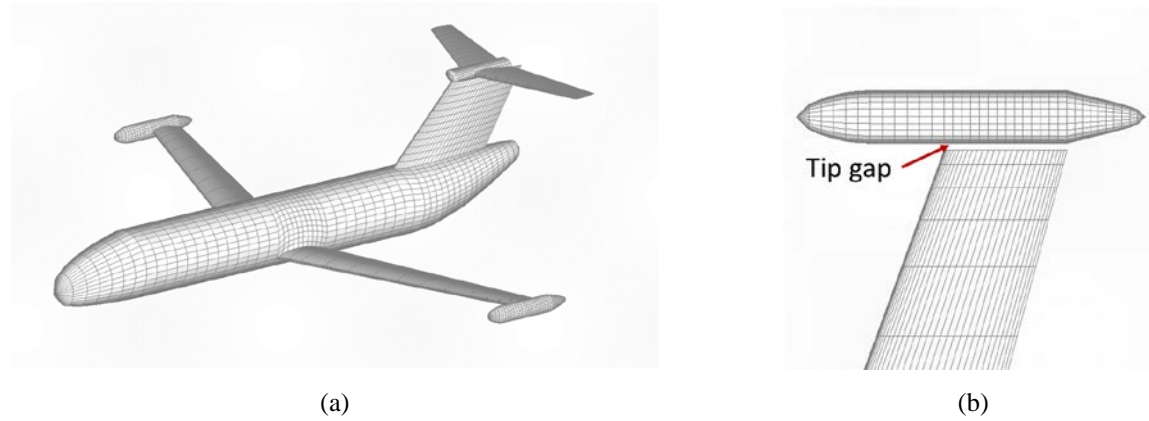
**Figure 5: Complete mesh (a) and detail of the gap between the wing tip and the pods (b).**

The Generalized Aerodynamic Force matrices were computed and substitued into NeoCASS to replace the ones computed with the DLM, hence it was possible to perform the flutter analysis in NeoCASS obtaining the V-f and V-g plots shown in Figure 6 to Figure 8. The flutter velocities for the three configuration considered and for both the aerodynamic methods are reported in Table 1.The structural matrices used for the flutter computation were the same ones obtained with the FEM and used for the flutter computation performed with the DLM in Sec. III-A
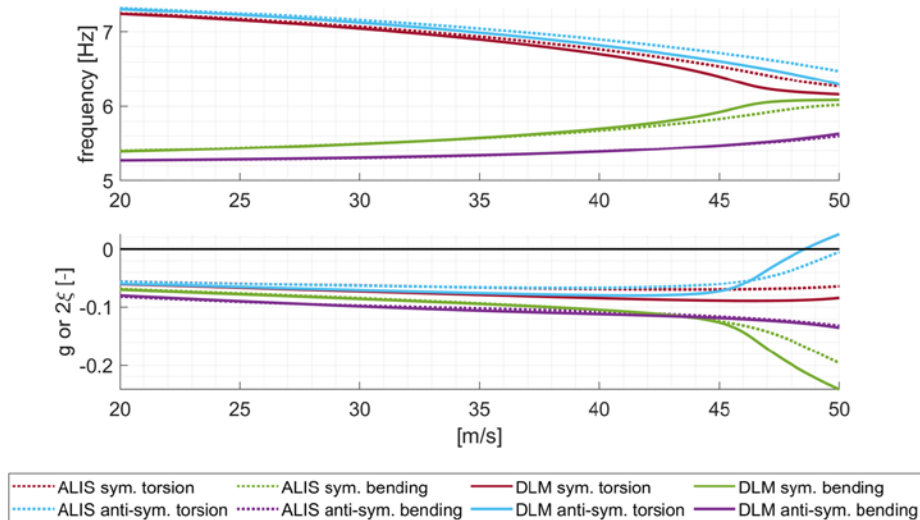
Figure 6: ALIS vs. DLM, without tip pods.
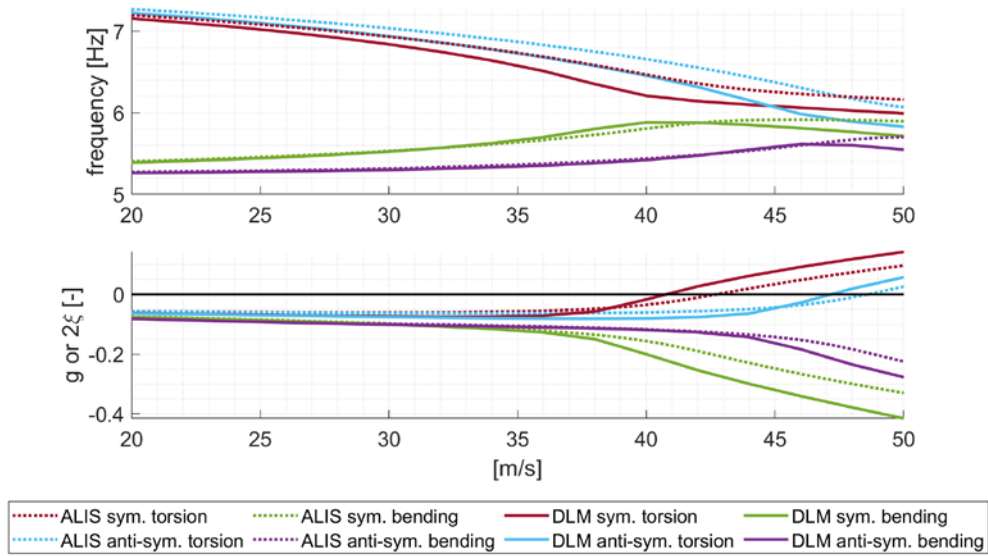
Figure 7: ALIS vs. DLM, with tip pods.
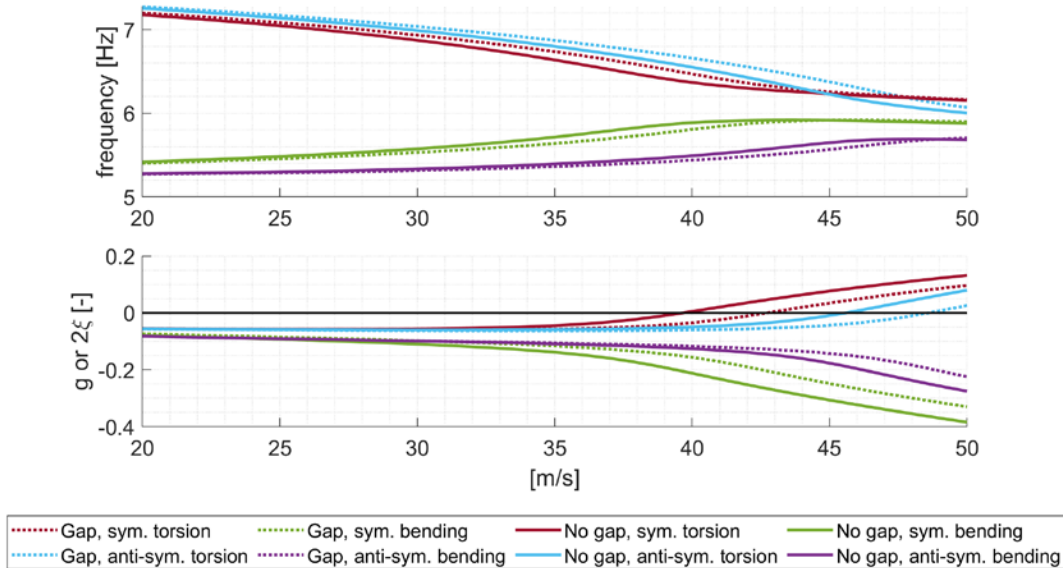
Figure 8: ALIS with and without gap between the wing tip and the pods.

Small differences in the flutter speeds can be noted between the two methodologies, with ALIS predicting the same flutter mechanism at higher speeds. Some geometrical and methodological differences are present for the two models: the DLM model was finetuned to match the flutter velocities measured in [2]-[5]. In the DLM model the flutter stopper pods were represented by crosses of two flat surfaces each while the ALIS mesh is based on the CAD model. Both aerodynamic modeling approaches capture the flutter phenomena in a very similar way. It is clear that the flutter behavior for the X-DIA model is strongly influenced by the dynamics and aerodynamics induced by the tip pods.

Table 1: Flutter Velocities and Frequencies for different wing tip pods models, DLM vs. ALIS

	No Tip Pods				Tip Pods and No Gap				Tip Pods and Gaps			
Aerodynamics	DLM		ALIS		DLM		ALIS		DLM		ALIS	
Flutter Mechanism	V[m/s]	F[Hz]	V[m/s]	F[Hz]	V[m/s]	F[Hz]	V[m/s]	F[Hz]	V[m/s]	F[Hz]	V[m/s]	F[Hz]
Symmetric	-	-	-	-	41.0	6.17	42.8	6.32	39.7	6.38	42.8	6.32
AntiSymmetric	48.8	6.39	50.0	6.47	47.0	5.95	48.6	6.13	45.7	6.18	48.6	6.13

C. The Static Output Feedback (SOF) closed loop flutter case.

The SOF controller is a simple Static Output Feedback controller that uses pseudo-integrated accelerations [4]-[5][20] to generate aileron commands through a gain matrix. The accelerations used are the ones measured on the leading edges of the wing tips and the outputs are the commands to the ailerons. With this layout, the gain matrix dimensions, Noutput x Ninput, are 2x2. The most general formulation for such controller scheme is the one in Eq.(**1**), while its Simulink implementation is illustrated in Figure 9.

$$\begin{Bmatrix} \delta_{rh} \\ \delta_{lh} \end{Bmatrix} = \begin{bmatrix} g_{rr} & g_{rl} \\ g_{lr} & g_{ll} \end{bmatrix} \begin{Bmatrix} \dot{x}_{rh\ tip} \\ \dot{x}_{lh\ tip} \end{Bmatrix} \tag{1}$$
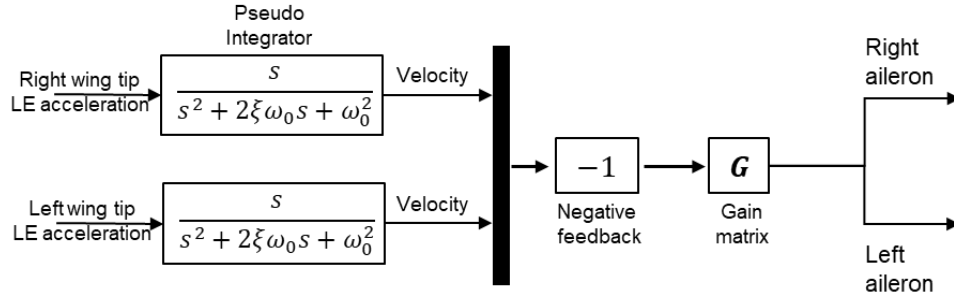
Figure 9: Block diagram of the closed loop flutter.

D. Symmetric SOF flutter control

Following the approach used for the previous wind tunnel tests (when the model was suspended on cables, [2]-[5]) a symmetric controller was implemented. In this case the aileron command is symmetric and computed from the mean value of the tips leading edge velocities, obtained through integration of the measured accelerations. Recalling Eq. (1), $g = g_{rr} = g_{rl} = g_{lr} = g_{ll} = 0.25$ and the control surface rotations requested are defined as in Eq.(2)

$$\delta_{rh} = \delta_{lh} = g(\dot{x}_{rh\ tip} + \dot{x}_{lh\ tip}); \boldsymbol{G} = \begin{bmatrix} 0.25 & 0.25 \\ 0.25 & 0.25 \end{bmatrix} \tag{2}$$

This controller already proved its robustness and capability of suppressing symmetric flutter in past X-DIA tests, and this is true also for this new case where the symmetric flutter is pushed to 53m/s. The controller is completely ineffective in stabilizing the anti-symmetric flutter. When the mode is anti-symmetric the mean value of the acceleration is null, and the control input is consequently null. This is shown in Figure 10 where it is possible to see how the anti-symmetric torsional mode eigenvalues are unmodified by the symmetric SOF controller. The square markers indicate the open loop eigenvalues while the plus marker indicates the close loop eigenvalues, the velocity is mapped by the color-bar and the stars markers indicates multiple of 10 m/s in the range between 10 and 60 m/s.
Hence, despite the symmetric flutter that is moved by active control to 53m/s, the first flutter of the closed loop system becomes the anti-symmetric bending at 47m/s. This allows us to control a single flutter mechanism (symmetric) without modifying the behavior of the second flutter mechanism (antisymmetric). It makes it possible,

then, to "fly" the model in closed loop using the symmetric AFS law up to the 2nd flutter speed (antisymmetric) and experimentally characterize the second flutter mode.

The SOF controller was designed at 45m/s to guarantee a 10% increment of the open loop flutter speed (41m/s), and then it was numerically tested up to an airspeed of 60m/s. No gain scheduling was necessary to stabilize the system over this speed range.
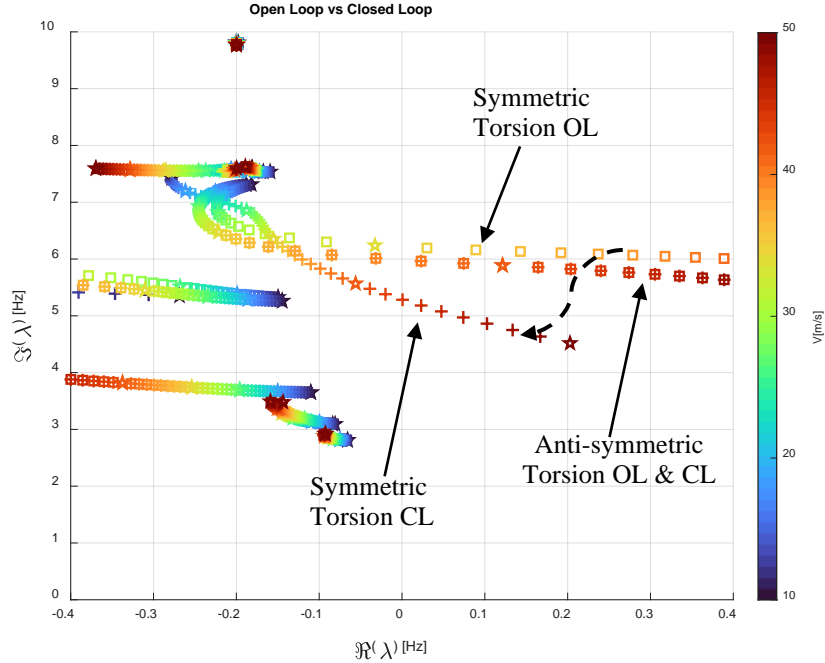
Figure 10: Open vs. Closed loop Root Locus: symmetric case (with active control focused only on the symmetric mechanism).

E. Anti-symmetric SOF flutter control

In this case the gain matrix is modified to decouple the controller between the left wing and right wing input/output actions. This means that the control required for each aileron is proportional to the acceleration measured on the same semi-wing. This simple modification to the gain matrix structure makes it possible to have the same performances as the symmetric controller concerning the control of symmetric modes, but thanks to the co-located layout it can suppress the antisymmetric modes as well. Recalling Eq. (1), $g = g_{rr} = g_{ll} = 0.5$; $g_{lr} = g_{rl} = 0$ and the control surface rotations requested are defined as in Eq.(3).

$$\begin{cases} \delta_{rh} = g\dot{x}_{rh\,tip} \\ \delta_{lh} = g\dot{x}_{lh\,tip} \end{cases}; \boldsymbol{G} = \begin{bmatrix} 0.5 & 0 \\ 0 & 0.5 \end{bmatrix} \tag{3}$$

The controller stabilizes the symmetric flutter up to 53m/s exactly as in the previous case, and it stabilizes the anti-symmetric mode (2nd flutter) across all the velocity range considered for the test (10-60m/s).

The numerical results of this controller are presented in Figure 11: the symmetric torsion flutter is suppressed exactly as in Figure 10, while in this case the anti-symmetric associated pole is always on the left of the imaginary axis of the Gauss plane, showing how the de-coupled controller stabilizes this mode as well.

As a drawback, this controller loses the redundancy obtained with the symmetric one, where in case of loss of one accelerometer the cross effect due to the mean value partially compensates for a sensor failure moving both the aileron of half the deflection obtained for the operative case.
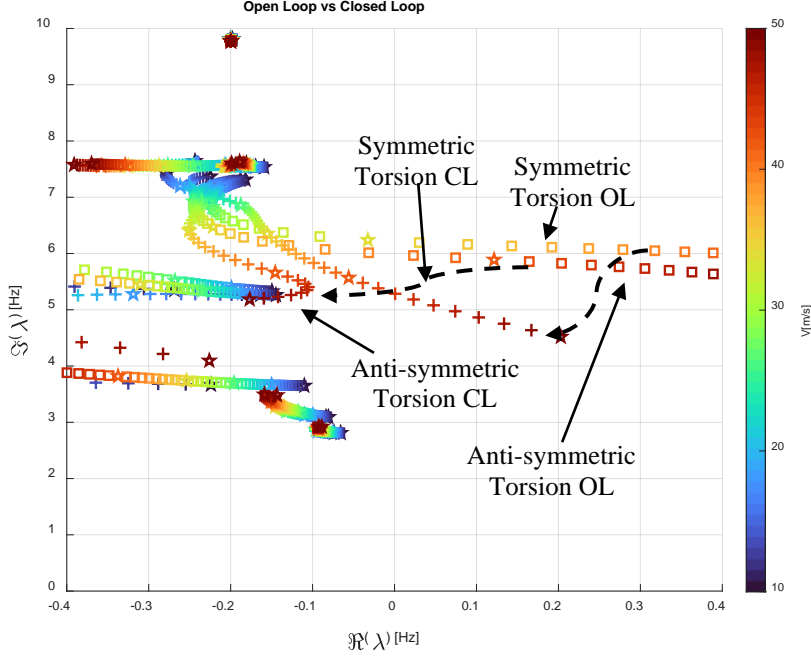
Figure 11: Open vs. Closed loop Root Locus: antisymmetric case.

F. The ILAF controller (Identical Location of Accelerations and Forces) – The symmetric case

The Identical Location of Accelerations and Forces (ILAF) control strategy has a long history of use in modal suppression and active flutter suppression [3][4][21]-[23]. As the theory states, if a force is applied proportional to but with opposite sign to a measured velocity (or integrated acceleration) at the location of the measurement, then the damping of all structural modes will increase. As used in the present case, the ILAF controller simply integrates the measured acceleration using a second order band-pass structure, whereby frequencies lower and higher than the flutter frequency range are attenuated. Additional compensation was added during tuning on the Nichols plot with the goal of achieving stability margins of approximately ± 8 dB in gain margin and $\pm 60°$ in phase margin. The final ILAF control structure is as follows:

$$C_{ILAF}(s) = K \cdot \frac{s}{s^2 + 1.6(.5\omega_f)s + (.5\omega_f)^2} \cdot \frac{s + 40}{s + 20} \cdot \frac{s^2 + 8s + 160000}{s^2 + 80s + 160000}$$

where ω_f is the flutter frequency. The final controller can be seen as a second order band-pass combined with a lag filter and a notch filter. The controller takes as input the four wing-tip accelerometers, located on leading and trailing edges, and provides the same output command to each aileron. The locations of the sensed velocities and the application of the aileron generated forces are close but not identical, as has been the case to date with most applications of ILAF laws to flutter suppression. The active control here, therefore, is focused on symmetric flutter mechanisms. Figure 12 shows the loop transfer function, where all the margins are highlighted.
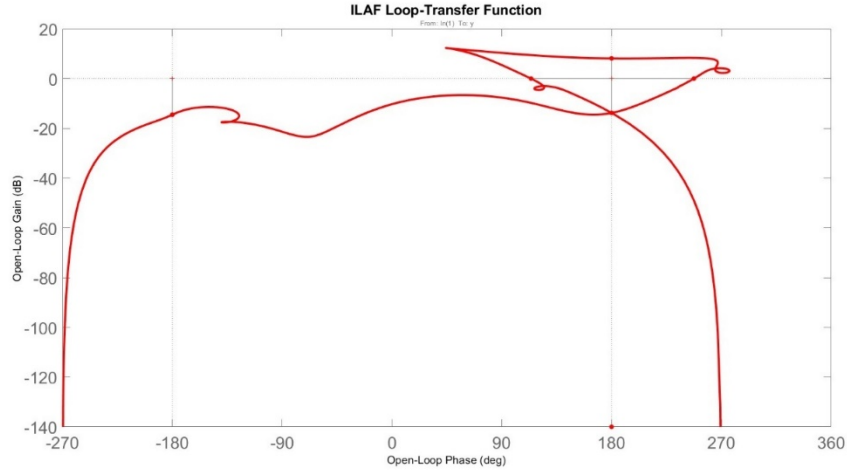
Figure 12: Nichols plot of the symmetric ILAF controller case showing stability margins at 42 m/s.

The closed-loop root locus, Figure 13, shows the symmetric ILAF controller to stabilize the symmetric flutter to approximately 44 m/s.
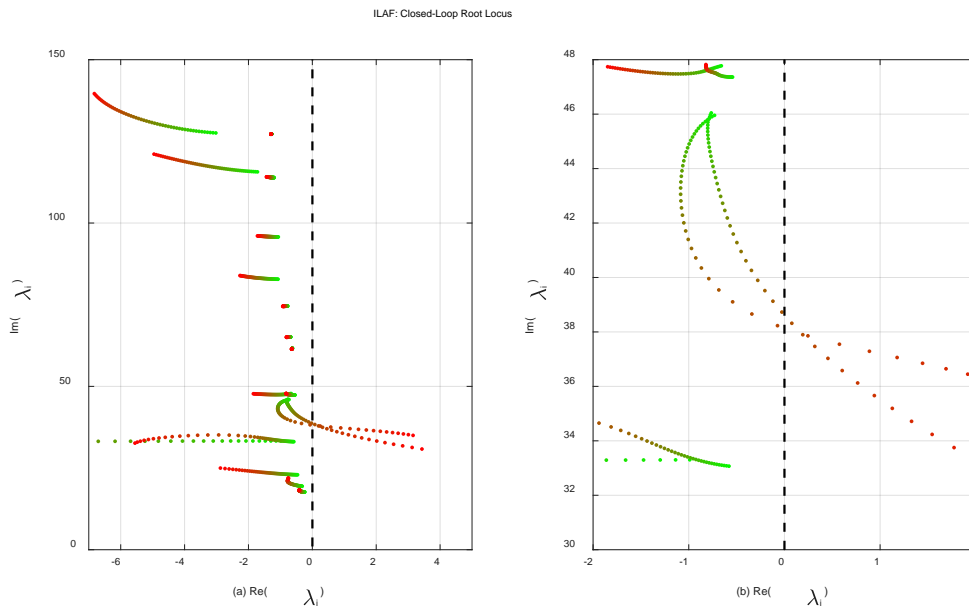
Figure 13: Closed-loop root locus for the symmetric ILAF controller for speeds of 10 m/s to 60 m/s. Enlarged view in (a) and close-in view in (b).

The goal with the ILAF controller was to pass the symmetric flutter speed and get as close as possible to the antisymmetric flutter mechanism to allow estimation of the dynamic system very near or at the antisymmetric flutter speed (Recall, that the presence of the flutter stoppers provided protection against any damage to the model if flutter amplitudes grew too much).

IV. Experimental Results

Tests with the X-DIA model on the pylon were carried out at the Politecnico di Milano (POLIMI) large wind tunnel (See [4] for description of a previous phase of testing in that tunnel). Different control laws can be uploaded to the onboard wind tunnel model computer for execution during the closed loop tests. Throughout the testing, at constant

speeds while increasing speed in speed increments, symmetric and antisymmetric excitation sweeps by the ailerons were used for gathering experimental I/O information.

A. Open loop flutter identification

The X-DIA aero-servo-elastic model was installed in the middle of the POLIMI's large wind tunnel test section and the airflow was increased by 5m/s steps until the open loop flutter speed was reached and the flutter stopper mechanism was automatically engaged. From numerical simulations and previous experimental campaign, the flutter speed was predicted to be slightly above 40 m/s, and so above this speed the next velocity step increments were 1m/s. The excitation was provided by a symmetric and linear aileron sweep command (Eq.(4)), with a frequency content between $f_0 = 4Hz$ and $f_1 = 14Hz$ and a duration on $T = 45s$ (Figure 14). The measurements were acquired for 3 repetitions of the input signal, with a rest time of 10s between each sweep. A trigger signal is used to identify the two ends of the sweep signal. This way it was possible to extract the time histories for times only when the excitation was active.

$$\delta_{cmd} = A \sin\left(2\pi\left(f_0 + \frac{f_1 - f_0}{T}t\right)t\right) \tag{4}$$
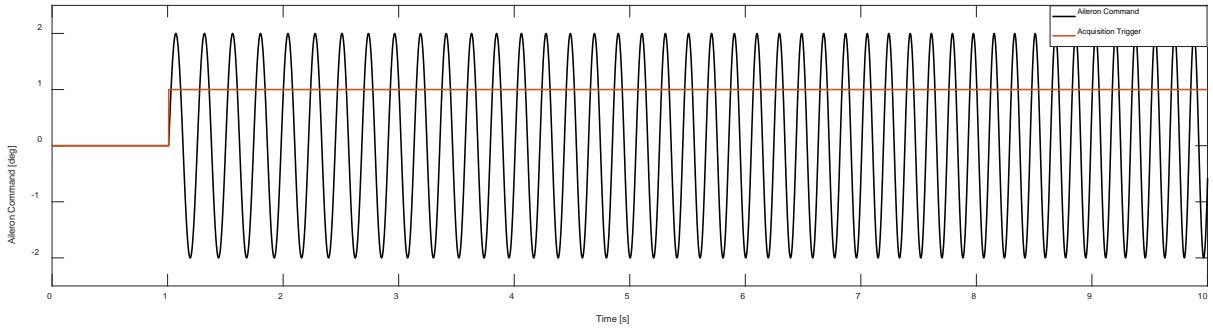
Figure 14: Zoom on the first 10 seconds of the excitation signal.

The acquired data were post-processed to get the Transfer Functions (TF) between the input and the output.
The transfer function can be estimated using two different estimators: H1 and H2 [24].

$$H1 = \frac{G_{xx}}{G_{yx}} \tag{5}$$

$$H2 = \frac{G_{xy}}{G_{yy}} \tag{6}$$

where, G indicates the Cross-Energy Spectral Density of the signals. If the subscripts are identical, e.g. "xx", G becomes an Energy Spectral Density. For the spectral analysis performed here, aiming to the evaluation of the H indicators, using the Energy or Power spectral density is the same, since both coherence and H indicators are obtained as a ratio between the energy or power spectra.

$$G_{xx} = |X|^2; G_{yy} = |Y|^2; G_{xy} = XY^* \tag{7}$$

Where the superscript * indicates the conjugate.
The capital letters (X,Y) indicate the sum of the Fourier transforms (FT) of the input signal x: $x(t) \xrightarrow{FT} \tilde{x}(f)$ and the of the output signal y: $y(t) \xrightarrow{FT} \tilde{y}(f)$ for the three excitation repetitions.

$$X = \sum_{i=1}^{N_{avg}} \tilde{x}_i \; ; \; Y = \sum_{i=1}^{N_{avg}} \tilde{y}_i \tag{8}$$

The coherence between the two signals is defined as:

$$\gamma_{xy} = \sqrt{\frac{|G_{xy}|^2}{G_{xx}G_{yy}}} \tag{9}$$

H1 and H2 are numerical arrays with sizes (Nf x Noutput x Ninput) with Nf being the number of frequencies used. The difference between them indicates the uncertainty band where the real transfer function H lies: H1 underestimates the transfer function (TF) by cleaning the noise on the output, while H2 overestimates the TF by cleaning the noise on the input signal. The coherence indicates how causal the system is, i.e. whether the output is due to the input (Figure 15)
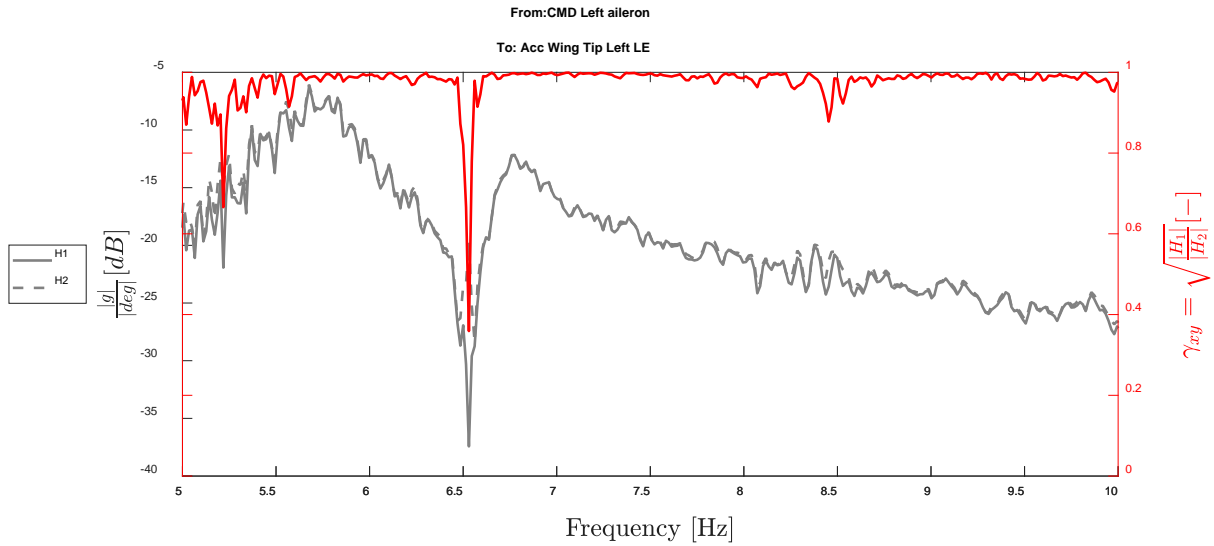
Figure 15: H1 and H2 estimators for the TF between the left aileron's excitation command and the left-wing tip leading edge accelerometer. In red the coherence between the two signals at V=35m/s.

This is true when the flow velocity is far from the flutter condition, i.e. 10 to 30 m/s. Not surprisingly, when the overall damping in the system goes down as the speed is increased into the 35-40 m/s range and more and more response is due to just the response of a low-damped system to the natural turbulence of the tunnel, the relative contribution of the aileron excitation to the response becomes smaller, and a drop in the coherence function around the flutter frequency appears. This is less evident in the H2 estimator which is less sensitive to the input noise.
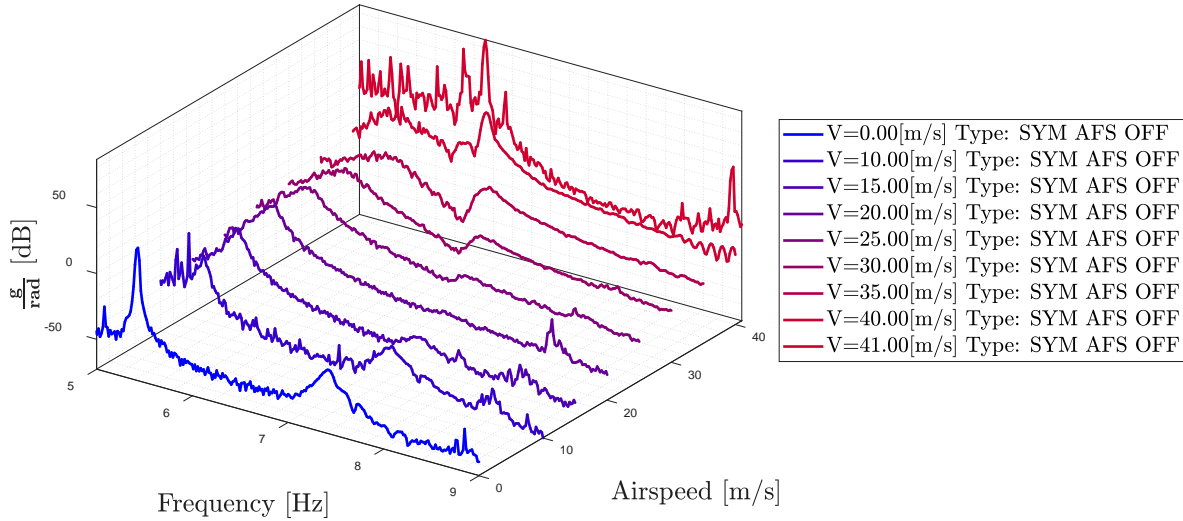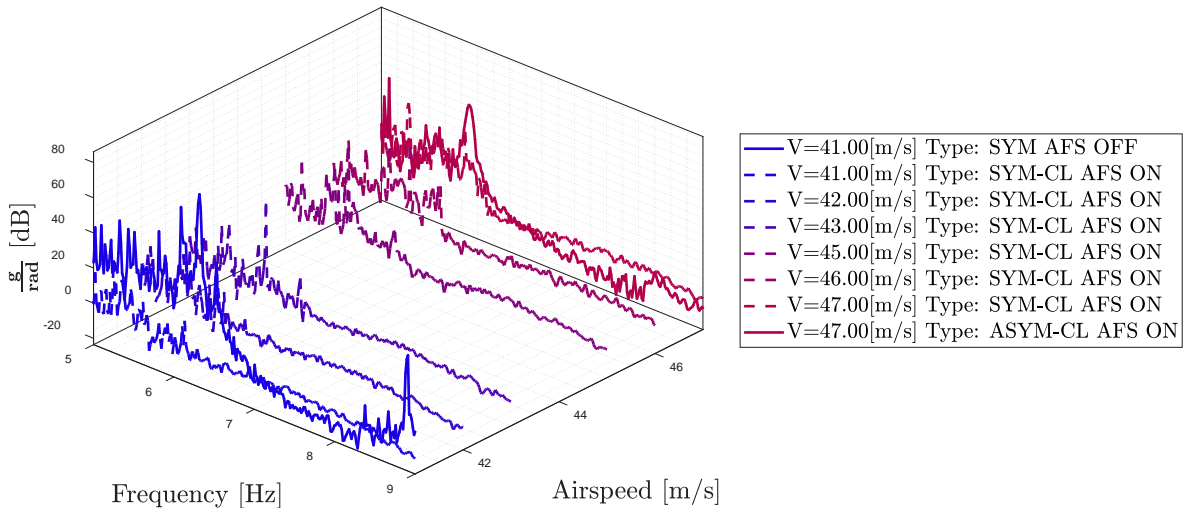
Figure 16: FRFs for different wind tunnel speeds – open loop.

Open loop frequency response curves (FRF) for the open loop case as functions of speed are shown in Figure 16.

B. SOF Closed loop symmetric flutter suppression AND anti-symmetric flutter identification

The identification technique described in the previous section is used for the anti-symmetric mechanism as well. In this case the symmetric flutter suppression controller is engaged and is allowed to fly the model beyond the symmetric flutter point. Since the controller acts symmetrically, it does not modify the behavior of the anti-symmetric flutter mechanisms. What is presented next are measurements in the range of $40\frac{m}{s} < V_\infty < 47\frac{m}{s}$ - that is, the airspeed range between the symmetric and antisymmetric flutter mechanisms.

Some stability checks for the symmetric controller at lower speeds were performed. Once confirmed that the controller was efficient also below 1st flutter speed, the model was flown beyond the 1st flutter point, increasing the airflow with 1m/s increments until reaching the 2nd flutter speed where the anti-symmetric flutter appeared. At that speed (actually, just slightly below it, but with significant model response already) the excitation was performed with both symmetric and anti-symmetric aileron sweeps. The anti-symmetric sweep (Figure 17) clearly identifies the anti-symmetric torsional mode peak at a frequency higher than the 1st torsion controlled mode.

Figure 17: FRFs for different wind tunnel speed (with symmetric AFS engaged).
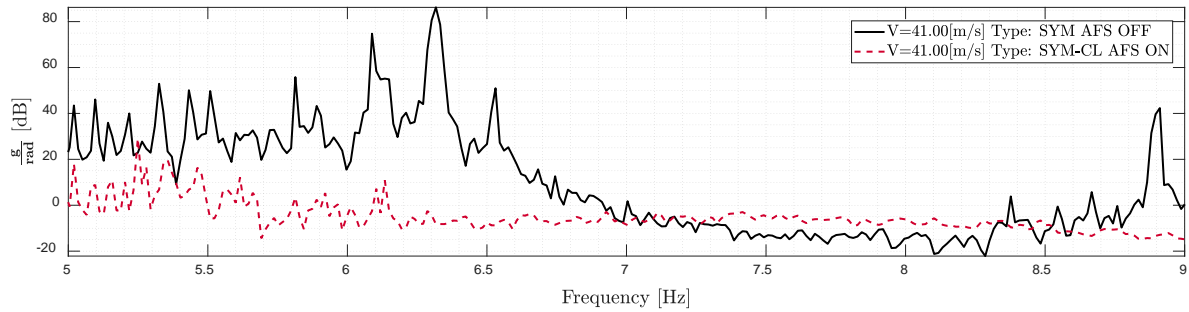
Figure 18: Open and closed loop FRFs at the symmetric flutter point (symmetric aileron excitation and symmetric SOF controller).
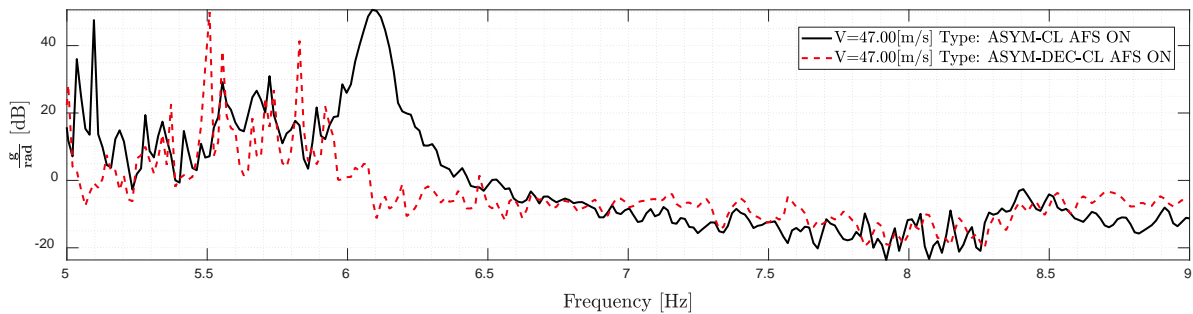

Figure 19: Open and closed loop FRFs at the antisymmetric flutter point (antisymmetric aileron excitation and anti-symmetric SOF controller).

C. SOF Closed loop flutter suppression of symmetric and anti-symmetric flutter

Finally, the SOF anti-symmetric flutter controller described above was tested, increasing the speed to 50m/s. Transfer functions are shown in Figure 18 Figure 19. The peak of the first flutter mechanism is flattened by the symmetric SOF controller, showing that the symmetric behavior is unmodified by the anti-symmetric controller. Moreover, the decoupled SOF controller can suppress the second flutter mechanism up to a tested airspeed of 50m/s. Test were stopped at this speed due to wind tunnel limitation, but numerically the closed loop system is stable up to 53 m/s.

D. Test results with the ILAF symmetric controller

The ILAF controller, in a nominal configuration, successfully suppressed flutter up to a speed of 45 m/s and with a gain increase of 1.5, suppressed flutter until the antisymmetric flutter mode emerged at 47 m/s. Figure 20, below, shows a verification of the stability properties of the ILAF controller in the nominal configuration for speeds of 30 m/s, 42 m/s, and 45 m/s.
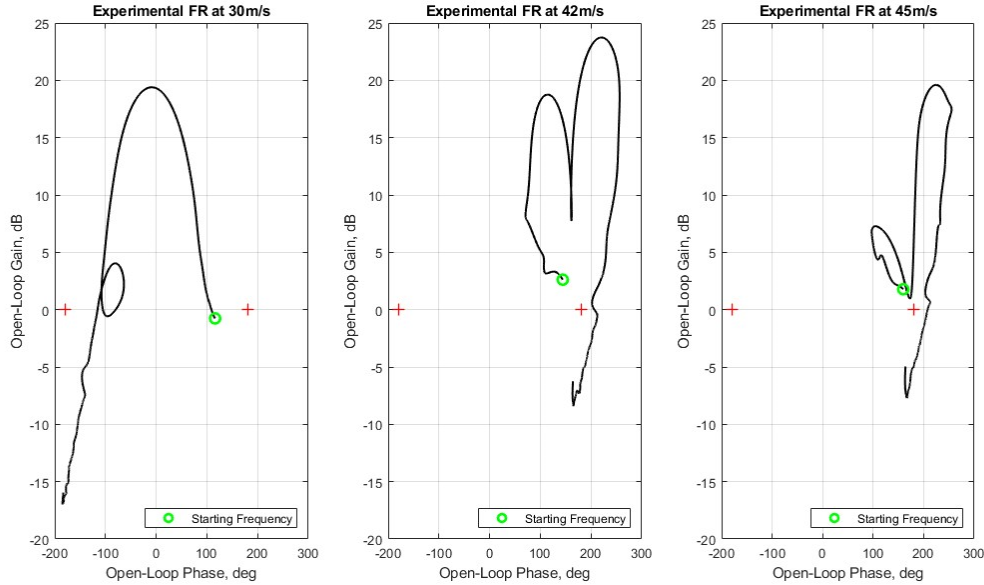
Figure 20: Experimental frequency response used to verify stability margins of the ILAF controller. The starting frequency, highlighted with the green circle, is 4 Hz and the ending frequency is 14 Hz.

Though stable up to a speed of 45 m/s, Figure 20 shows a general trend of decreasing stability margins as the speed increased.

V.   Conclusions

The paper presents new Active Flutter Suppression (AFS) results with the modified X-DIA aeroservoelastic model [4][5] in the POLIMI large low-speed wind tunnel. In a change from the support of the model by a cable system in earlier tests, the model was now mounted on a pylon/strut system. The two lowest speeds flutter mechanisms in the wind tunnel operative range involved bending / twisting of the wing, one symmetric and one antisymmetric. . It was demonstrated that with simple AFS control laws it was possible to stabilize the symmetric instability, pass it when tunnel speed was increased, and reach the second instability – the first antisymmetric flutter – at a higher speed.

System identification I/O runs just below the symmetric flutter speed and then just below the antisymmetric flutter speed (made possible by a "symmetric" controller that does not affect antisymmetric dynamics) made it possible to gather important experimental results that can be used for fine tuning the state space model of the system to capture accurately both flutter mechanisms.

Comparing the two controllers used – the SOF and ILAF controllers – both controllers, in the symmetric operation mode, were able to pass the symmetric flutter mechanism when the speed increased and bring the system to just below the antisymmetric flutter speed. To suppress flutter beyond the antisymmetric flutter speed, a dedicated SOF controller was used and was successful in stabilizing the system (beyond two flutter mechanisms) up to the maximum speed that the test covered in the tunnel.

The paper presents work that demonstrates how, using active flutter suppression, experimental i/o results can be obtained close to or at flutter mechanism speeds that are beyond the first flutter speed - In the case here, the utilization of symmetric and antisymmetric AFS. With the growing availability of multiple control surfaces on active flexible wind tunnel and flight vehicle systems, active control has the potential to allow reaching multiple flutter mechanisms in tests safely. Work that demonstrates such techniques and capabilities will be presented in subsequent papers.

References

[1] Livne, E, "Aircraft Active Flutter Suppression: State of the Art and Technology Maturation Needs", Journal of Aircraft, Vol. 55, No. 1, Jan.-Feb. 2018, pp. 410-452, doi: 10.2514/1.C034442

[2] Ricci, S., Marchetti, L., Riccobene, L., De Gaspari, A., Toffol, F., Fonte, F., Mantegazza, P., Berg, J., Morgansen, K., and Livne, E., "An Active Flutter Suppression (AFS) Project: Overview, Results and Lessons Learned", AIAA Paper 2021-0908, doi: 10.2514/6.2021-0908

[3] Berg, J., Morgansen, K., and Livne, E., Fonte, F., Toffol, F., De Gaspari, A., Marchetti, L., Ricci, S., and Mantegazza, P., "Analytical and Experimental Evaluation of Multivariable Stability Margins in Active Flutter Suppression Wind Tunnel Tests", AIAA Paper 2021-1261, doi: 10.2514/6.2021-1261

[4] Marchetti, L., Toffol, F., De-Gaspari, A,, Fonte, F., Riccobene, L., Ricci, S., Mantegazza, P., Berg, J., Livne, E., and Morgansen, K., "The Development of a Wind Tunnel System for Active Flutter Suppression Research: Overview and Insights", AIAA Journal, 2022,, Vol. 60, No. 12, pp. pp. 6692–6714, doi: 10.2514/1.J061985

[5] Ricci, S., Toffol, F., De Gaspari, A., Marchetti, L., Fonte, F., Riccobene, L., ... & Morgansen, K. (2022). Wind Tunnel System for Active Flutter Suppression Research: Overview and Insights. AIAA Journal, 60(12), 6692-6714. https://doi.org/10.2514/1.J061985

[6] Fonzi, N., Ricci, S., & Livne, E. (2023, June). Experimental Studies of the Effect of Preload on Freeplay-Induced LCO. In ASME Aerospace Structures, Structural Dynamics, and Materials Conference (Vol. 87141, p. V001T02A013). American Society of Mechanical Engineers.

[7] Fonzi, N., Ricci, S., & Livne, E. (2023). New insights on limit cycle oscillations due to control surface freeplay. MATERIALS RESEARCH PROCEEDINGS, 37, 38-41.

[8] Fonzi, N., Curasi, H., Ricci, S., & Livne, E. (2022). Experimental Studies on Dynamic Freeplay Nonlinearity. In 19th International Forum on Aeroelasticity and Structural Dynamics (IFASD 2022) (pp. 1-20).

[9] Kholodar, D., and Dowell, E. H., "Behavior of Airfoil Section with Control Surface Freeplay for Nonzero Angles of Attack," AIAA Journal, Vol. 37, No. 5, 1999, pp. 651–653, doi:10.2514/2.766

[10] Chen, P.C. and Lee, DF.H., "Flight-Loads Effects on Horizontal Tail Free-Play-Induced Limit Cycle Oscillation", Mar.-Apr. 2008, Journal of Aircraft, Volume 45, Issue 2, pp. 478-485, doi.org/10.2514/1.29611

[11] Tang, D., and Dowell, E.H., "Aeroelastic Airfoil with Free Play at Angle of Attack with Gust Excitation", Feb. 2010, AIAA Journal, Volume 48, Issue 2, pp. 427-442, doi: 10.2514/1.44538

[12] Chen, P.C., Ritz, E., and Lindsley, N., "Nonlinear Flutter Analysis for the Scaled F-35 with Horizontal-Tail Free Play", April 2014, Journal of Aircraft, Volume 51, Issue 3, pp. 883-889, doi: 10.2514/1.C032501

[13] De Gaspari, A., Mannarino, A., and Mantegazza, P., "A Dual Loop Strategy for the Design of a Control Surface Actuation System with Nonlinear Limitations," Mechanical Systems and Signal Processing, Vol. 90, June 2017, pp. 334–349, Doi:10.1016/j.ymssp.2016.12.037

[14] Cavagna, L., Ricci, S., and Riccobene, L., "A Fast Tool for Structural Sizing, Aeroelastic Analysis and Optimization in Aircraft Conceptual Design", AIAA Paper 2009-2571, doi: 10.2514/6.2009-2571

[15] Ripepi, M., & Mantegazza, P. (2013). Improved matrix fraction approximation of aerodynamic transfer matrices. AIAA journal, 51(5), 1156-1173.

[16] Nastran, M. S. C. (2004). Basic dynamic analysis user's guide. MSC. Software Corporation. USA.

[17] Beckert, A., & Wendland, H. (2001). Multivariate interpolation for fluid-structure-interaction problems using radial basis functions. Aerospace Science and Technology, 5(2), 125-134.

[18] Mantegazza, P. & Cardani C. (1978). Continuation and direct solution of the flutter equation. Computers & Structures, 8(2), 185-192.

[19] Bindolino, G., and Paolo, M. "Improvements on a Green's function method for the solution of linearized unsteady potential flows." Journal of aircraft 24.6 (1987): 355-361.

[20] Fonte, F., Ricci, S., and Mantegazza, P., "Gust Load Alleviation for a Regional Aircraft Through a Static Output Feedback", 2015, September-October, Journal of Aircraft, Volume 52, Issue 5, pp. 1559-1574, doi: 10.2514/1.C032995

[21] Wykes, J., and Mori, A., "Techniques and Results of an Analytical Investigation into Controlling the Structural Modes of Flexible Aircraft", AIAA Paper 1965-1140, doi: 10.2514/6.1965-1140

[22] Wykes, J., "Structural dynamic stability augmentation and gust alleviation of flexible aircraft", AIAA Paper 1968-1067, doi: 10.2514/6.1968-1067

[23] Schmidt, D.K., "Stability Augmentation and Active Flutter Suppression of a Flexible Flying-Wing Drone", Journal of Guidance, Control, and Dynamics, 2016, Volume 39, Issue 3, March, pp. 409-422, doi: 10.2514/1.G001484

[24] Heylen, W., Lammens, S., & Sas, P. (1997). Modal analysis theory and testing (Vol. 200, No. 7). Leuven, Belgium: Katholieke Universiteit Leuven.